PAPER

Check for updates

Green synthesis and magnetothermal performance of Zn₁₋ₓONiₓ nanocomposites for magnetic hyperthermia applications

Sellemhe Brahim Salem,[a] Mohammed Ould M'hamed, [ID] *[a] Khalidou Ba,[b] Turki Altoub,[c] Ali Z. Alanzi,[d] O. M. Lemine[c] and Mohamed Said Mohamed Sidya[a]

Nickel-doped zinc oxide ($Zn_{1-X}ONi_X$, $X = 0.05–0.20$) nanocomposites were synthesized *via* a simple and eco-friendly co-precipitation route and systematically investigated for their structural, thermal, magnetic, and magnetothermal properties. X-ray diffraction confirmed the hexagonal wurtzite phase at low Ni concentrations (≤5%), while weak NiO reflections emerged above 10%, revealing a solubility limit for Ni incorporation. Thermal analysis (TGA/DSC) indicated high stability above 450 °C with distinct exothermic crystallization associated with Ni incorporation. FTIR spectra confirmed Zn–O stretching vibrations along with hydroxyl and carbon-related groups. Magnetic measurements revealed weak room-temperature ferromagnetism, with the highest saturation magnetization of 0.117 emu g⁻¹ for $Zn_{0.85}ONi_{0.15}$, indicating optimal Ni substitution and defect-mediated exchange interactions. Under an alternating magnetic field (160 Oe, 468 kHz), $Zn_{0.85}ONi_{0.15}$ dispersions achieved a therapeutic hyperthermia threshold of 42 °C, with a specific absorption rate (SAR) of 9.2 W g⁻¹. These results demonstrate that $Zn_{1-X}ONi_X$ nanocomposites exhibit a relatively good magnetothermal response under an AMF, which needs to be optimized through polymeric surface functionalization and measurement under different frequency and field amplitudes.

1. Introduction

Metal and metal oxide nanoparticles (NPs) have emerged as versatile platforms in electronics, catalysis, energy storage, and biomedical sciences.[1,2] Among them, zinc oxide (ZnO) has been extensively investigated due to its unique combination of physical, chemical, and biological properties.[3]

As a II–VI semiconductor, ZnO exhibits exceptional electrical and optical characteristics, including high transparency, a wide direct band gap of 3.37 eV, and a large exciton binding energy of 60 meV, making it highly suitable for optoelectronic and photonic applications.[4–6] The morphology of ZnO is a critical factor influencing its surface area, surface energy, and crystallographic orientation, thereby modulating its performance in various technological applications. ZnONPs can be engineered in multiple morphologies—such as nanowires, nanorods,

nanobelts, nanosheets, nanoparticles, and hierarchical architectures—each conferring distinct physicochemical properties.[7–11]

Tailoring ZnO properties through doping has proven to be an effective strategy to enhance its structural and optical properties, and induce ferromagnetism. For instance, transition metal dopants such as manganese (Mn), cobalt (Co), and nickel (Ni) introduce localized states within the bandgap, thereby modifying the conductivity, magnetic ordering, and optical absorption behaviour.[12]

Nickel-doped ZnO nanoparticles (NPs) have attracted considerable attention for applications in solar cells, gas sensors, photocatalysis, hydrogen production and antibacterial systems, as well as in spintronic devices.[13–19] These studies have clearly shown that Ni incorporation into the ZnO lattice significantly modifies its optical, electronic, magnetic and catalytic properties, thereby broadening the functional scope of ZnO-based nanomaterials.

Despite these advances, the magnetothermal properties of Ni-doped ZnO nanostructures under alternating magnetic fields (AMF) remain unexplored. This represents a critical limitation, particularly in view of the growing interest in magnetothermal effects for biomedical applications such as magnetic hyperthermia (MH) and magnetically assisted drug delivery.[20,21] In MH, heat generated by magnetic nanoparticles exposed to an AMF is used to selectively induce cytotoxic effects in cancer

[a] Unité de Chimie Verte, de Valorisation des Bioressources et de l'Environnement (UC2VBE), Département de Chimie, Faculté des Sciences et Techniques, Université de Nouakchott, Mauritania. E-mail: m.mhamed@univ-nkc.mr; medabdelwedoud@gmail.com

[b] Unité de recherché: Chimie des Matériaux, Département de Chimie, Faculté des Sciences et Techniques, Université de Nouakchott, Mauritania

[c] Magnetic Materials Lab (MML), Department of Physics, College of Sciences, Imam Mohammad Ibn Saud Islamic University (IMSIU), Riyadh 11623, Saudi Arabia

[d] Microelectronics and Semiconductors Institute, King Abdulaziz City for Science and Technology (KACST), Riyadh, Saudi Arabia

cells, which are more sensitive to temperatures in the range of 40–45 °C than healthy tissues.[22] The heating efficiency is quantified by the specific absorption rate (SAR), defined as the thermal energy dissipated per unit time and per unit mass of magnetic material.[23] It is well established that the heating performance of magnetic nanoparticles under AMF depends on a combination of intrinsic and extrinsic parameters, including particle size, morphology, crystallinity, magnetic properties (such as saturation magnetization, coercivity, magnetic anisotropy, and Curie temperature), particle concentration, surface modification, and the amplitude and frequency of the applied magnetic field.[21,23] To date, iron oxide nanoparticles have been the most widely investigated materials for MH due to their low toxicity, superparamagnetic behaviour, relatively high SAR values.[24] Nickel-based nanomaterials have also been explored, particularly nickel ferrites and nickel-based alloys, due to their enhanced magnetic anisotropy and tunable magnetic response.[25,26] Regarding $ZnO_{1-X}Ni_X$ nanocrystalline, previous studies have primarily focused on dilute magnetic semiconductor behaviour at low Ni contents, with focuses on the understanding of the origin of room temperature ferromagnetism (RTFM).[13] Addressing this gap is essential for establishing clear structure–magnetism–magnetothermal correlations and for enabling the design of ZnO/Ni nanostructures for advanced biomedical applications.

In the present study, we report the controlled synthesis of $Zn_{1-X}ONi_X$ nanoparticles ($X = 0.05, 0.10, 0.15,$ and 0.20) via a simple, efficient, and environmentally method. The synthesized nanomaterials were comprehensively characterized to elucidate the influence of Ni incorporation on their structure and magnetic behaviour.

Unlike prior investigations that primarily emphasized the optical, electronic, or catalytic properties of ZnO/Ni nanostructures, this work provides one of the first systematic assessments of their magnetothermal performance as a function of Ni concentration. By directly linking dopant incorporation to structural and magnetic responses, our study introduces new insights into the tunability of ZnO-based nanomaterials and expands their potential utility in next-generation applications such as magnetic hyperthermia, spintronic devices, and magnetically driven energy conversion.

2. Experimental part

2.1. Materials

All chemicals used in this study were of analytical grade and procured from Merck; they were used without any further purification. Double-distilled water and ethanol were employed for washing and purifying the final product. Zinc acetate dihydrate $[Zn(CH_3COO)_2 \cdot 2H_2O]$ and nickel acetate dihydrate $[Ni(CH_3COO)_2 \cdot 4H_2O]$ served as the metal ion precursors. Ni-doped ZnO nanoparticles were synthesized via a coprecipitation method, adapted with slight modifications from the procedure reported in ref. 27. The nanoparticles were prepared with four different Ni doping concentrations ($X = 5\%$, 10%, 15%, and 20%) by varying the precursor concentrations accordingly.[28]

2.2. Preparation of $Zn_{1-X}ONi_X$ nanocrystalline

$Zn(CH_3COO)_2 \cdot 2H_2O$ and $Ni(NO_3)_2 \cdot 2H_2O$ are dissolved in deionized water under continuous magnetic stirring for 40 minutes at room temperature. Subsequently, a 2 M NaOH solution was added dropwise to the mixture to adjust the pH to approximately 10. The reaction was then stirred for an additional hour to facilitate the formation of a precipitate. The resulting product was collected by filtration, thoroughly washed with deionized water and ethanol, and finally calcined at 400 °C for 4 hours (Fig. 1).

2.3. Characterization

X-ray diffraction (XRD) patterns were recorded on a PROTO Benchtop powder diffraction system equipped with CuKα radiation source ($\lambda = 1.5418$ Å) and under the operating conditions: voltage of 30 V, current of 20 A, and power of 0.6 kW. The patterns were recorded in the 2θ range 20–80° using a scan rate of 0.015°. The average crystallite size is deduced from the XRD by Scherrer formula:

$$D = \frac{K\lambda}{B \cos(\theta)} \quad (1)$$

where $\lambda = 1.54178$ Å, D crystallite size, K is a constant whose value is approximately 0.9 and B (rad) is the full width at half maximum (FWHM) of a diffraction peak.

FTIR spectra were recorded using INFRALUM FT-08 ALU-MEX in the wavenumber range 400–4000 cm^{-1}. Morphological observation and chemical composition were performed using SEM-SERON TECHNOLOGIES (Model, AIS 1800C) and TEM (Type JEOL-JEM 1400 operating at 120 kV). Vibrating sample magnetometer (VSM, model 7404) equipped with 1.8 T magnet was used for magnetic characterization at room temperature. The heating efficiency under an AMF was performed using a commercial system "Nanotherics Magnetherm".

All experiments were performed third times under identical experimental conditions to ensure reproducibility. The reported values for structural, magnetic, and magnetic hyperthermia measurements are expressed as the mean ± standard deviation (SD). Mean values were obtained by averaging the results of independent measurements, while the standard deviation was used to quantify data dispersion.

3. Results and discussion

3.1. Structure, morphology and chemical composition

The X-ray diffraction (XRD) patterns of undoped ZnO and Ni-doped ZnO nanoparticles shown in Fig. 2 confirm the formation of the hexagonal wurtzite structure, with diffraction peaks matching the JCPDS card no. 36-1451. The refined lattice parameters were calculated and summarized in Table 1. At low doping levels (5%), no additional diffraction peaks corresponding to Ni, NiO, or Zn–Ni phases were detected, indicating the effective incorporation of Ni^{2+} ions into the ZnO lattice without secondary phase formation. However, at higher doping concentrations ($X \geq 10\%$), additional weak peaks appeared at $2\theta = 38.11°$ (111) and $2\theta = 43.25°$ (200), which are assigned to
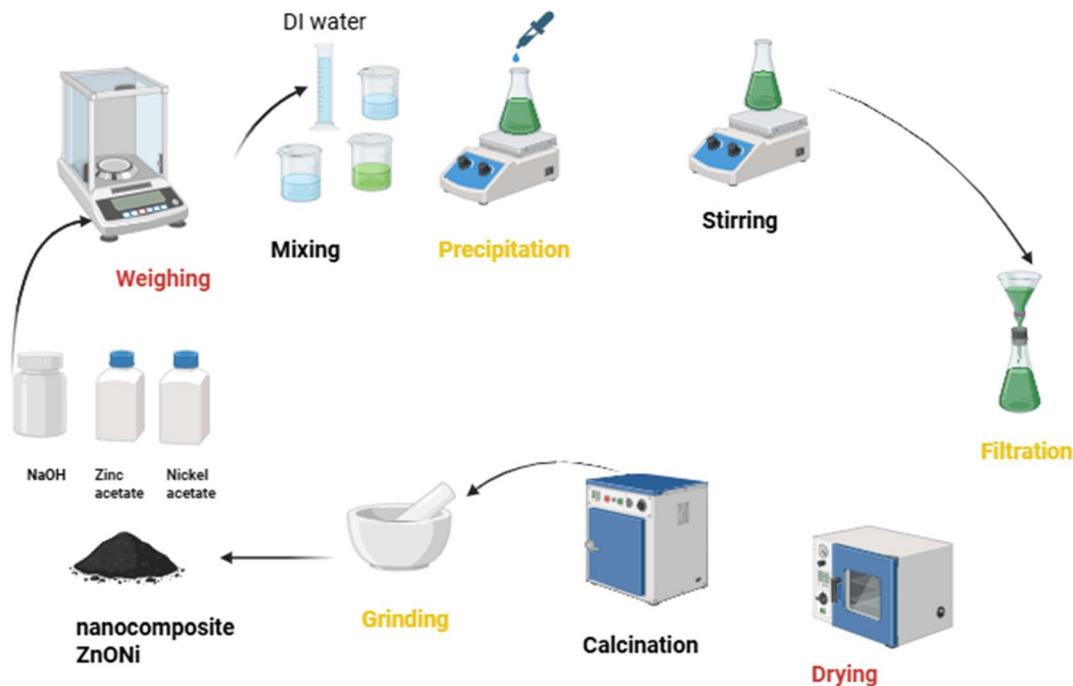
Fig. 1 Schematic representation of the $Zn_{1-X}ONi_X$ nanocrystalline's synthesis.
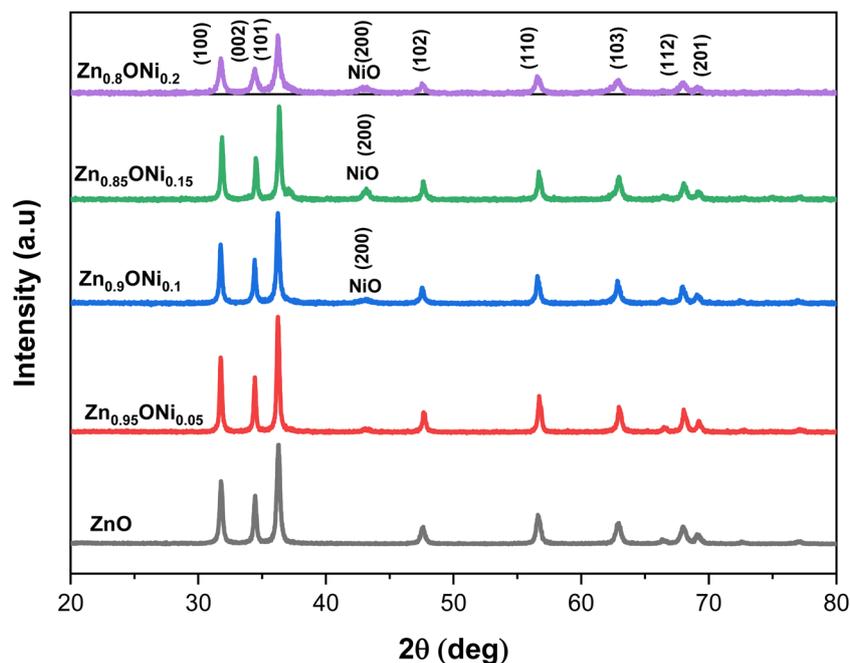

Fig. 2 Powder X-ray diffraction patterns of $Zn_{1-X}ONi_X$ nanocrystalline ($X = 0.05, 0.10, 0.15,$ and 0.20).

NiO. The intensity of these peaks increases with Ni content, suggesting that the solubility limit of Ni in ZnO is below 10%. Above this limit, phase segregation occurs, whereas at lower concentrations (5%), Ni^{2+} ions substitute Zn^{2+} sites while preserving the single-phase wurtzite structure, consistent with previous reports.[4] The average crystallite size was estimated using the Debye–Scherrer equation as indicated in Table 1. For pure ZnO, the crystallite size was ~36 nm, increasing to ~52 nm at 10% Ni doping, which suggests enhanced crystal growth at moderate doping concentrations. This effect may be attributed to the catalytic role of Ni^{2+} ions in promoting oriented growth within the ZnO lattice. In contrast, a significant reduction in crystallite size was observed at 20% Ni (~25 nm), which can be explained by increased lattice strain and the inhibition of

Table 1 Lattice parameters and crystallite size

Samples	a (Å)	c (Å)	Unit cell volume (Å^3)	Average crystallite size (nm)
ZnO	3.24 ± 0.01	5.20 ± 0.01	47.57 ± 0.15	35.4 ± 2.1
$Zn_{0.95}ONi_{0.05}$	3.25 ± 0.01	5.21 ± 0.01	47.70 ± 0.16	53.4 ± 2.8
$Zn_{0.9}ONi_{0.1}$	3.25 ± 0.01	5.21 ± 0.01	47.73 ± 0.16	43.8 ± 2.4
$Zn_{0.85}ONi_{0.15}$	3.24 ± 0.01	5.27 ± 0.01	48.08 ± 0.18	49.6 ± 2.6
$Zn_{0.8}ONi_{0.2}$	3.25 ± 0.01	5.21 ± 0.01	47.68 ± 0.16	26.4 ± 1.9

crystallite growth at higher doping levels. It can be seen also form Table 1 that unit cell volume increases and then decrease for Ni(20%). This at low levels of Ni doping, an increase in the unit cell volume of ZnO is often observed despite the slightly smaller ionic radius of Ni^{2+} (0.55 Å) compared to Zn^{2+} (0.60 Å). This apparent anomaly can be attributed to the incorporation of Ni ions into interstitial rather than substitutional sites, particularly at dilute concentrations.[13,14] Such incorporation introduces lattice strain and defect states—such as oxygen vacancies and zinc interstitials—which result in local lattice distortion and expansion. These defects may induce local lattice distortions and internal stress, which can lead to an initial increase in lattice parameters and unit cell volume. However, as the Ni concentration increases, substitutional doping becomes dominant, with Ni^{2+} ions (0.55 Å) replacing Zn^{2+} ions (0.60 Å) at tetrahedral sites in the ZnO lattice. Owing to the smaller ionic radius of Ni^{2+} compared to Zn^{2+} in four fold coordination, this substitution results in lattice contraction and a corresponding decrease in the unit cell volume. Moreover, the formation of secondary phases NiO, which have different crystal structures and lattice parameters, induces changes in the composition and microstructural properties, which might contributes also to this reduction.

The surface morphology and microstructure of the synthesized nanocrystalline were examined *via* scanning electron microscopy (SEM), as shown in Fig. 3. The images reveal different patterns indicating that the surface morphology depends on the concentration of Ni. Energy-dispersive X-ray spectroscopy (EDX) was employed to verify the purity and elemental composition of the Ni-doped ZnO nanoparticles ($Zn_{1-X}ONi_X$). The analysis indicates the presence of Zn, Ni, and O as the main elements across all samples, confirming the absence of impurities. Furthermore, the Ni-to-Zn atomic ratios (Ni/Zn) were calculated as 0.0033, 0.0631, 0.0996, and 0.1319 for the 5%, 10%, 15%, and 20% Ni-doped samples, respectively. These values closely match the nominal stoichiometric ratios used during synthesis, demonstrating the precision and reliability of the doping process. The TEM image of $Zn_{0.8}ONi_{0.2}$ nanocrystalline exhibits a typical quasi-spherical morphology with corresponding narrow size distributions, indicating the monodispersity and uniformity of the sample (Fig. 4a). An average diameter of 67 nm is deduced from particle size distribution histogram as shown in Fig. 4b.

3.2. Thermal analysis by TGA/DSC

The thermal stability of $Zn_{1-X}ONi_X$ nanocrystalline ($X = 0.05$ and 0.20), nanocrystalline was systematically examined by thermogravimetric analysis (TGA) coupled with differential scanning calorimetry (DSC). The TGA/DSC profiles are presented in Fig. 5a and b and the results are summarized in Table 2. For $Zn_{0.95}ONi_{0.05}$ and as indicate in Fig. 5a, the TGA curve shows a minor initial weight loss of ~1–1.5% below 150 °C, which is attributed to the evaporation of residual solvents and physically adsorbed water molecules. A subsequent weight loss of ~1.5–2% occurs in the range of 250–400 °C, corresponding to the thermal decomposition of nickel acetate precursors ($Ni(CH_3COO)_2 \cdot 4H_2O$) and due to Ni incorporation into the ZnO lattice. Beyond 450 °C, the TGA curve becomes stable, indicating the completion of the decomposition process and the formation of the final ZnO : Ni phase. The associated DSC signal exhibits a weak exothermic feature near 200–250 °C, assigned to the combustion of residual organics, followed by a sharp exothermic peak between 330–350 °C, consistent with the crystallization of Ni-doped ZnO. No additional thermal events are observed above 400 °C, confirming the stability of the system. For $Zn_{0.80}ONi_{0.20}$ (Fig. 5b), the TGA curve displays a more gradual weight loss of ~1.5–2% between 100–300 °C, attributed to the removal of adsorbed water and the decomposition of residual nickel-based organic species. A pronounced mass-loss feature centered near 300 °C indicates the rapid breakdown of nickel acetates and the crystallization of Ni-enriched ZnO (ZnONi). Above 400 °C, the weight stabilizes, evidencing the formation of a thermally robust crystalline phase. The DSC profile reveals a double exothermic feature between 280–320 °C: the first peak corresponds to the oxidation/combustion of organic residues, while the second is associated with the crystallization of ZnO doped with 20% Ni. The absence of thermal events beyond 400 °C further confirms the complete formation and thermal stability of the crystalline ZnONi phase.

3.3. FTIR results

Fourier-transform infrared (FTIR) spectroscopy was used to investigate the functional groups and chemical bonding in undoped and Ni-doped samples. Fig. 6 shows the FTIR transmission spectra of the nanocrystalline, recorded in the range of 500–4000 cm^{-1}. All spectra display several characteristic absorption bands. The broad band observed around 3100–3700 cm^{-1} is attributed to the stretching vibration of O–H bonds associated with surface hydroxyl groups (–OH) on ZnO nanoparticles, which are commonly related to adsorbed water or hydroxyl species.[29] The bands appearing at 1463 cm^{-1}, 1641 cm^{-1}, and 2341 cm^{-1} are assigned to vibrations of C–H and C=C groups.[30,31] Their presence indicates trace amounts of
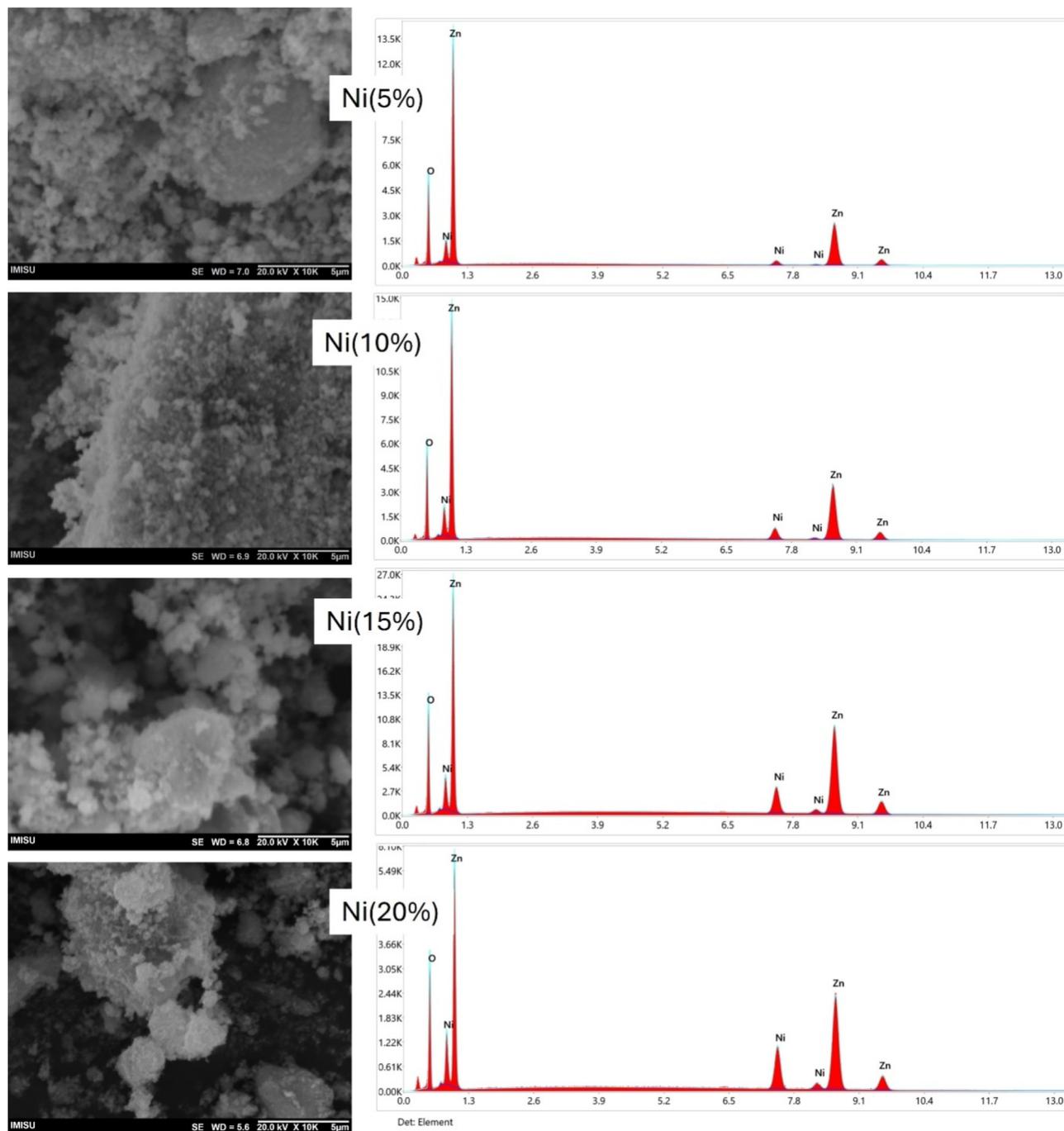
Fig. 3 SEM and EDAX analysis of the $Zn_{1-X}ONi_X$ nanocrystalline ($X = 0.05$, 0.10, 0.15, and 0.20).

residual carbon-containing species originating from the organic precursors used during synthesis. In nanocrystalline oxide systems, such residual organics can persist after calcination due to strong adsorption on high-surface-area particle surfaces, particularly when the thermal treatment is insufficient to completely eliminate all carbonaceous fragments. This effect is more pronounced at higher Ni contents, where local structural disorder may further hinder complete decomposition. In addition, the absorption band observed at approximately 853 cm^{-1} can also be attributed to minor carbon-related residues rather than to a secondary crystalline impurity phase. In general, metal oxides such as ZnO exhibit characteristic absorption bands below 800 cm^{-1}, arising from interatomic lattice vibrations.[32,33] Accordingly, the region between 445 and 540 cm^{-1} corresponds to Zn–O stretching vibration modes, which are a distinctive feature of nanocrystalline ZnO.[31]

3.4. Magnetic measurements

Fig. 7a displays the magnetization (M–H) curves of Ni-doped ZnO nanocrystalline samples measured at 300 K under
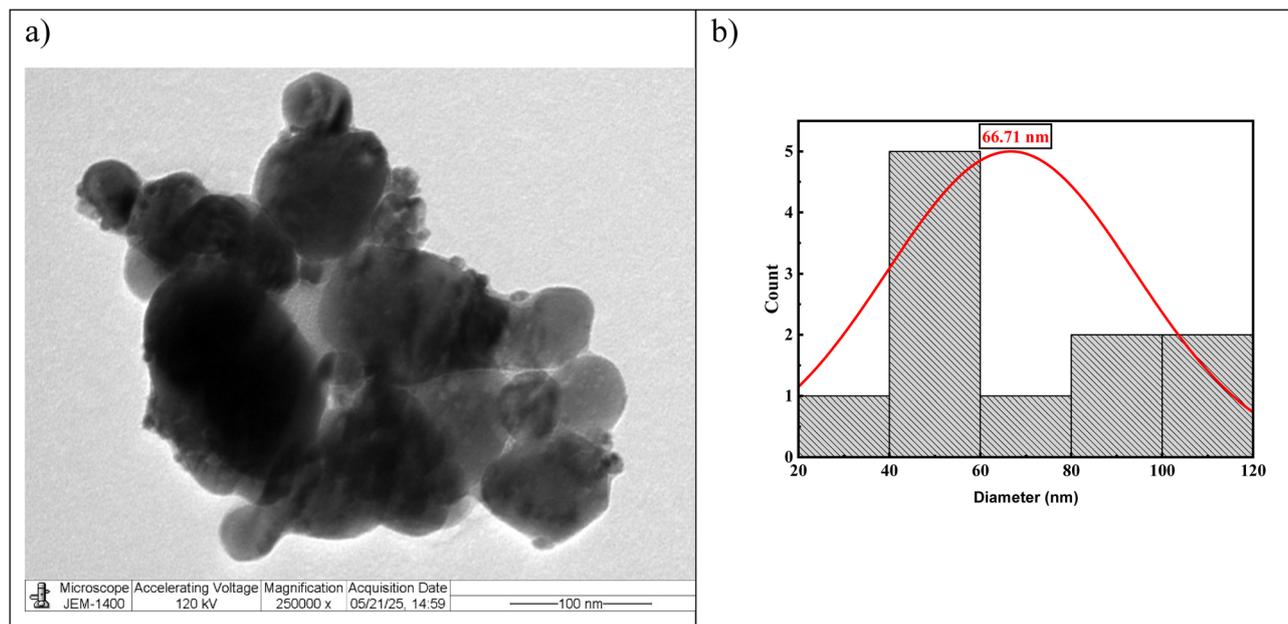
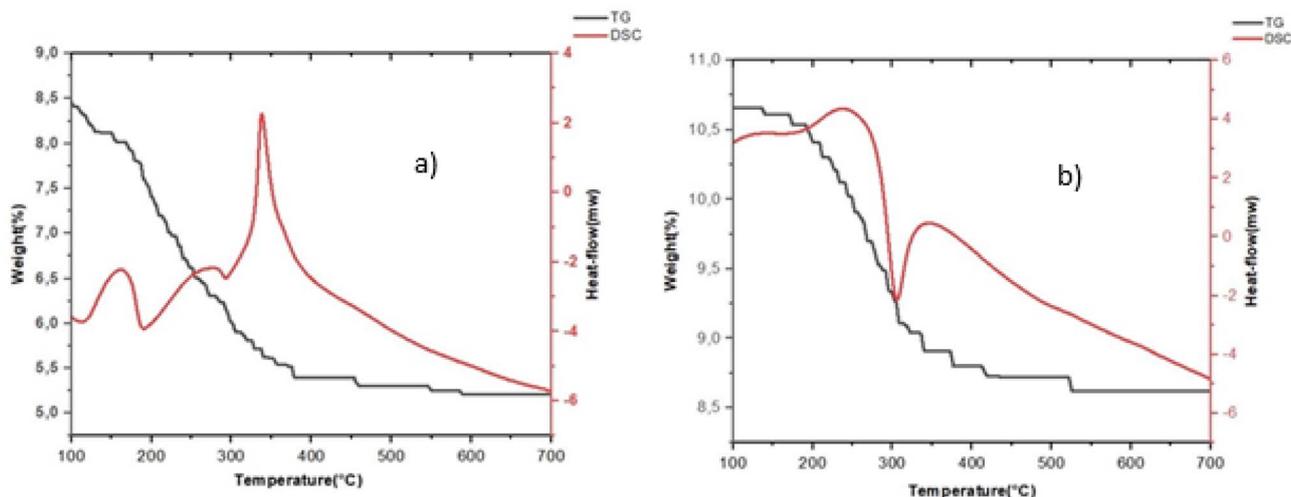**Fig. 4** (a) TEM image of $Zn_{0.80}ONi_{0.2}$ and (b) corresponding particle–size distributions.

Fig. 5 TGA and DSC of (a) $Zn_{0.95}ONi_{0.05}$ and (b) $Zn_{0.8}ONi_{0.2}$.

varying applied magnetic fields. All samples exhibit a weak room temperature ferromagnetism (RTFM), as evidenced by the characteristic S-shaped hysteresis loops, low values of coercivity and remanence (Table 3). The extracted M_s values are 0.032, 0.059, 0.117, and 0.085 emu g^{-1} for Ni doping levels of 5%, 10%, 15%, and 20%, respectively. The origin of RTFM in Ni-doped ZnO has been the subject of intense debate and several mechanisms have been proposed in the literature to explain this phenomenon:[34–36] (i) magnetic impurity incorporation: Ni^{2+} ions, with their unpaired 3d electrons, substitute Zn^{2+} sites within the ZnO lattice. This substitution introduces localized magnetic moments that can couple *via* exchange interactions, resulting in long-range ferromagnetic ordering. (ii) Secondary phase contributions: XRD analysis confirmed the presence of weak NiO-related peaks at higher doping levels (≥10%). Since NiO is an antiferromagnet in bulk form, its behaviour in nanoscale and defect-rich environments can deviate significantly, occasionally contributing to a weak ferromagnetic signal. (iii) Intrinsic defect mediation: oxygen vacancies (V_O) and zinc interstitials (Zn_i) in the ZnO lattice are known to play a crucial role in mediating magnetic interactions. Defect states near the conduction band can facilitate carrier-mediated exchange (bound magnetic polarons), enhancing the magnetic coupling between Ni ions.

Interestingly, the non-monotonic evolution of M_s with Ni concentration is observed as shown in Fig. 7b. The M_s increases

Table 2 Summary of thermal analysis (TGA/DSC) of $Zn_{1-X}ONi_X$ nanocrystalline ($X = 0.05$ and 0.20)

Sample	Weight loss (%)	Temperature range (°C)	DSC event(s)	Assigned process
$Zn_{0.85}ONi_{0.15}$	~1–1.5%	<150	—	Evaporation of residual solvents and adsorbed water
	~1.5–2%	250–400	Minor exothermic (~200–250 °C); strong exothermic (330–350 °C)	Combustion of residual organics; crystallization of Ni-doped ZnO
	Stable	>450	—	Formation of thermally stable crystalline phase
$Zn_{0.8}ONi_{0.2}$	~1.5–2%	100–300	—	Desorption of water and decomposition of organic species (nickel acetates)
	Pronounced loss	~300	Double exothermic (280–320 °C)	Combustion of organics; crystallization of ZnONi (20% Ni)
	Stable	>400	—	Fully formed and thermally stable crystalline phase
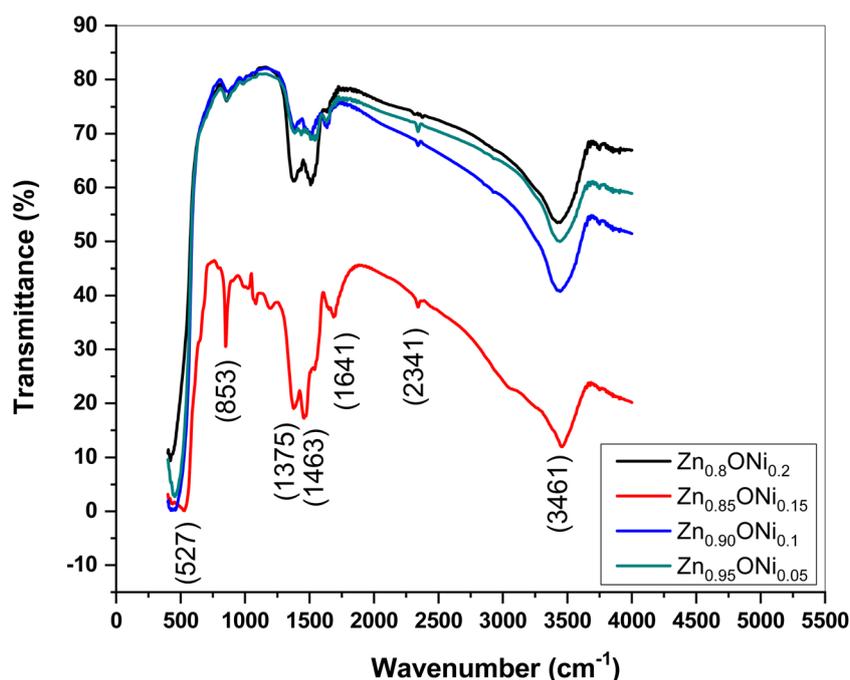
Fig. 6 FTIR transmission spectra of $Zn_{1-X}ONi_X$ nanocrystalline ($X = 0.05$, 0.10, 0.15, and 0.20).

significantly from 0.032 emu g^{-1} (5% Ni) to a maximum of 0.117 emu g^{-1} (15% Ni), reflecting the efficient incorporation of Ni^{2+} into the ZnO lattice and enhanced exchange interactions at intermediate doping levels. However, at 20% Ni doping, M_s decreases to 0.085 emu g^{-1}. This reduction may be attributed to excess of Ni incorporation, which can lead to antiferromagnetic super exchange between adjacent Ni^{2+} ions, competing with ferromagnetic interactions and reducing net magnetization.

3.5. Magnetic hyperthermia study

Fig. 8a shows the temperature evolution under AMF of $Zn_{1-X}ONi_X$ nanocrystalline and NiO at AMF amplitude of 170 Oe and frequency of 468 kHz. Samples with high concentration of Ni

(15 and 20%) exhibit a significant temperature rise, while low concentration of Ni and NiO does not show a significant heating ability. $Zn_{0.85}ONi_{0.15}$ nanoparticles reach magnetic hyperthermia temperature (42 °C),which is essential for effective cancer treatment. Other samples does not attain hyperthermia temperature, indicating their limited heating efficiency under such conditions.

The amount of heat dissipated by magnetic nanoparticles under an AMF is generally defined by sample absorption rate (SAR), which is calculated by the following equation:

$$\text{SAR} = \frac{\rho C_w}{\text{mass}_{\text{MNP}}}\left(\frac{\Delta T}{\Delta t}\right) \qquad (2)$$
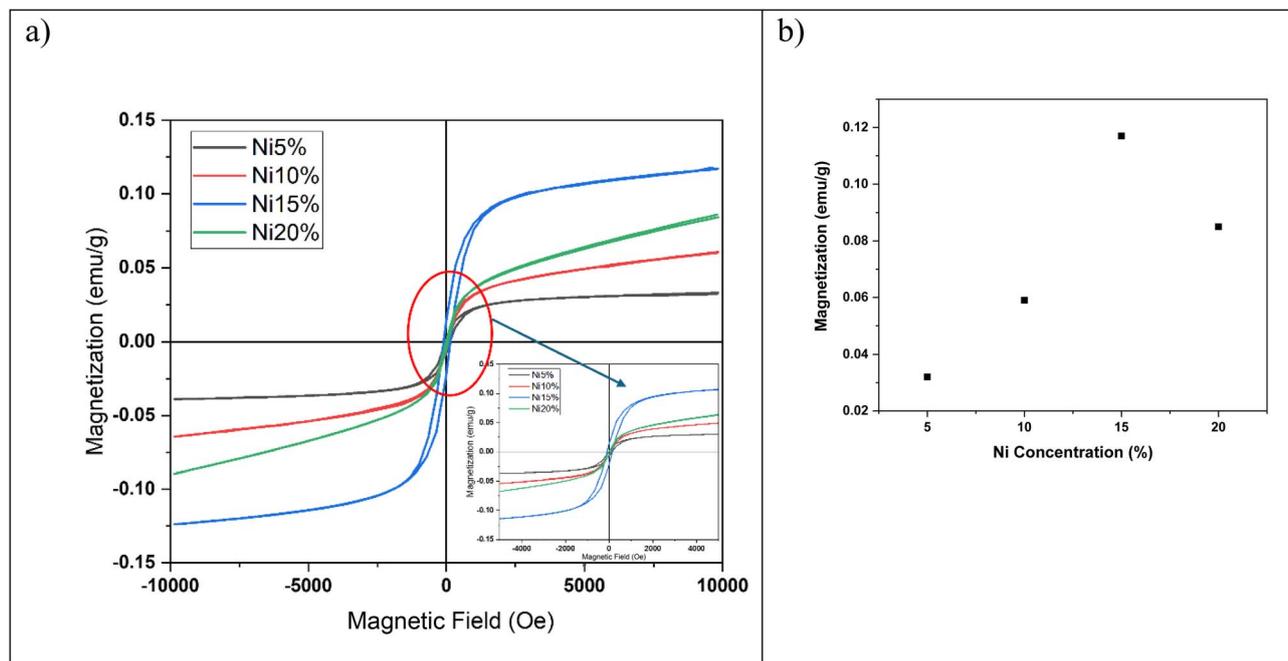
Fig. 7 (a) $M-H$ curves at room temperature (inset indicated the loop at low field) of $Zn_{1-x}ONi_X$ nanocrystalline ($X = 0.05$, 0.10, 0.15, and 0.20) and (b) evolution of saturation with Ni concentration.

Table 3 Magnetic parameters deduced from $M-H$ curves at room temperature

Samples	M_s (emu g^{-1})	H_c (Oe)	M_r (emu g^{-1})
$Zn_{0.95}ONi_{0.05}$	0.032 ± 0.003	26.2 ± 2.1	0.005 ± 0.001
$Zn_{0.9}ONi_{0.1}$	0.059 ± 0.004	134.4 ± 6	0.007 ± 0.001
$Zn_{0.85}ONi_{0.15}$	0.117 ± 0.006	146.1 ± 7.2	0.014 ± 0.002
$Zn_{0.8}ONi_{0.2}$	0.085 ± 0.005	164.3 ± 8.0	0.006 ± 0.001

where C_w is the specific heat capacity of water (4.185 J g^{-1} K^{-1}), ρ is the density of the colloid, mass$_{MNP}$ is the concentration of the magnetic nanoparticles in the suspension and $\frac{\Delta T}{\Delta t}$ represents the heating rate. By performing a linear fit of temperature increase *versus* time at the initial time interval (1 to ~30 s), the slope $\Delta T/\Delta t$ is obtained.

The calculated values of SAR are 5.22, 5.96, 9.2 and 6.8 (W g^{-1}) for $Zn_{0.95}ONi_{0.05}$, $Zn_{0.9}ONi_{0.10}$, $Zn_{0.85}ONi_{0.15}$ and $Zn_{0.80}ONi_{0.2}$, respectively (Fig. 8b). The highest value is obtained for $Zn_{0.85}ONi_{0.15}$ nanocrystalline (9.2 W g^{-1}) correlates with its higher magnetization, consistent with the strong dependence of SAR on intrinsic magnetic parameters such as saturation magnetization, coercivity, and remanence. Morphological aspects (particle size distribution, degree of agglomeration) and interparticle dipolar interactions are also key factors influencing the overall magnetothermal output.[37] The maximum SAR observed for Zn $_{0.85}ONi_{0.15}$ remains substantially lower those reported for other systems (see Table 3). However, it is essential to emphasize that direct comparisons of SAR values across different studies must be approached with caution, as SAR is not an intrinsic material property but rather a function of numerous experimental and physical variables. Critical

parameters influencing SAR include nanoparticle size and morphology, coating nature, magnetic anisotropy, and saturation magnetization, as well as external field parameters such as field amplitude (H), frequency (f). Additionally, calorimetric methods, sample holders, and data processing protocols vary across laboratories, contributing to systematic discrepancies in reported values.

For a more reliable comparison of heating efficiencies reported across different magnetic hyperthermia studies, the concept of Intrinsic Loss Power (ILP) has been introduced. Unlike the specific absorption rate (SAR), which is strongly influenced by experimental parameters such as field amplitude and frequency, ILP offers a normalized metric that facilitates objective evaluation of the intrinsic heating efficiency of magnetic nanoparticles.

It can be determined using the following expression:

$$ILP = SAR/fH^2 \qquad (3)$$

where SAR is the specific absorption rate (W g^{-1}), H represents the applied field amplitude (A m^{-1}), and f denotes the applied frequency (Hz).

The resulting ILP is expressed in nH m^2 kg^{-1} and reflects the intrinsic ability of MNPs to convert electromagnetic energy into heat, independent of the applied field conditions.

As shown in Table 3, the ILP values obtained for $Zn_{0.85}ONi_{0.15}$ NPs is low but in the range reported for commercial ferrofluids, which typically exhibit ILP values between 0.2 and 3.1 nH m^2 kg^{-1}.[26]

It is important to highlight that nickel exhibits inherent toxicity, which must be carefully considered when envisaging
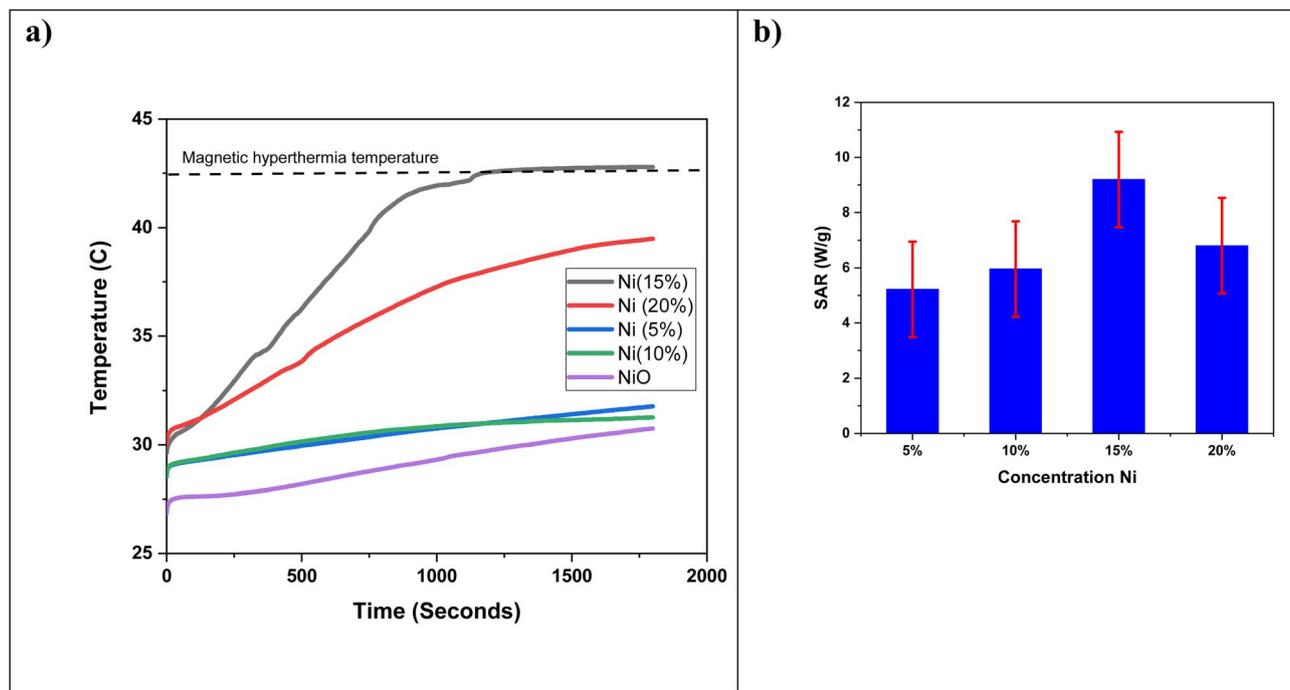
Fig. 8 (a) Temperature rise for $Zn_{1-x}ONi_x$ nanocrystalline and NiO and (b) corresponding SARs values.

biomedical applications. However, the biocompatibility of such nanocrystalline systems can be substantially improved through surface functionalization with well-established biocompatible polymers, such as chitosan, polyethylene glycol (PEG), dextran, or silica coatings. In addition to mitigating potential cytotoxic effects, surface functionalization plays a critical role in enhancing colloidal stability, particularly by suppressing aggregation arising from magnetic dipole–dipole interactions between nanoparticles.

In this context, $Zn_{0.85}ONi_{0.15}$ nanoparticles coated with chitosan are currently under investigation. The polymer shell is expected to improve dispersion stability, limit dipole–dipole-driven clustering, and thereby further enhance heating efficiency under an alternating magnetic field, ultimately making these nanostructures more suitable for prospective magnetic hyperthermia applications (Table 4).

4.   Discussion

XRD analysis confirms that all samples crystallize predominantly in the hexagonal wurtzite ZnO structure (JCPDS 36-1451).

At low Ni content ($X = 0.05$), no secondary phases are detected, indicating effective incorporation of Ni^{2+} ions into the ZnO lattice, consistent with earlier reports on dilute Ni-doped ZnO systems.[4] At higher Ni concentrations ($X \geq 0.10$), weak reflections attributed to NiO appear, revealing that the solubility limit of Ni in ZnO is exceeded and phase segregation occurs.

The lattice parameters and unit cell volume show a non-monotonic dependence on Ni content. Despite the smaller ionic radius of Ni^{2+} (0.55 Å) compared to Zn^{2+} (0.60 Å), an initial lattice expansion is observed at low and intermediate doping levels. This behavior is attributed to defect-induced lattice distortion associated with oxygen vacancies, zinc interstitials, and local strain generated during dopant incorporation.[13] At higher Ni content, substitutional incorporation of Ni^{2+} together with NiO formation promotes lattice contraction and partial strain relaxation. Previous reports indicate similar behavior for Ni doped ZnO nanocrystalline at low concentration of nickel.[14]

Thermal analysis indicates that precursor decomposition and crystallization of Ni-doped ZnO occur below 400 °C, while the absence of further thermal events confirms the formation of thermally stable crystalline phases. The more complex DSC

Table 4   Comparison of heating ability of $Zn_{0.85}ONi_{0.15}$ with different nanomaterials

Ferrofluids	Synthesis method	Frequency (kHz)	Field (mT)	SAR (W g^{-1})	ILP (nH m^2 kg^{-1})	References
$Zn_{0.85}ONi_{0.15}$	Co-precipitation	468	16	9.2	0.25	This work
Hydrothermal	Pyrrole–Fe$_3$O$_4$	472	17	53.77	0.46	38
Emulsion polymerization	Fe$_3$O$_4$–PDMAEMA	260	20.25	~25	~0.4	39
Co-precipitation	Fe$_3$O$_4$–chitosan	100	10–20	~20	~0.3	40
Hydrothermal	Fe$_3$O$_4$–PAA	332	17	36	0.59	41

features at higher Ni content are consistent with Ni-enriched ions and ZnO–NiO phase separation, corroborating the structural results.

FTIR spectra show characteristic Zn–O lattice vibrations together with O–H and weak carbon-related bands, attributed to surface hydroxyls and residual organic species commonly observed in nanocrystalline oxides with high surface area as reported previously.[29–33]

All Ni-doped samples exhibit weak room-temperature ferromagnetism. This behavior is consistent with defect-mediated magnetic coupling mechanisms proposed for Ni-doped ZnO, where localized magnetic moments from substitutional Ni^{2+} ions interact *via* intrinsic defects, often described by the bound magnetic polaron model.[34–36] The saturation magnetization increases up to $X = 0.15$ and then decreases at $X = 0.20$, reflecting an optimal balance between magnetic ion concentration and defect density, while higher Ni content promotes antiferromagnetic super exchange and NiO-related contributions that reduce net magnetization.[34–37] The magnetic hyperthermia response follows the same trend as the magnetic properties, with the highest SAR obtained for $Zn_{0.85}ONi_{0.15}$ nanocrystalline. Although SAR values are lower than those of iron-oxide-based ferrofluids, normalization using the intrinsic loss power (ILP) places the present system within the lower range reported for commercial ferrofluids.[26] This is expected given the dilute magnetic nature of ZnO-based systems and highlights the relevance of ILP for meaningful cross-study comparison.

5. Conclusion

In this work, $Zn_{1-X}ONi_X$ ($X = 0.05, 0.10, 0.15,$ and 0.20) nanocomposites were successfully synthesized *via* a simple and environmentally friendly co-precipitation method. Structural analysis confirmed the retention of the hexagonal wurtzite ZnO phase at low Ni concentrations ($\leq 5\%$), with secondary NiO phases emerging above 10% doping, reflecting a solubility threshold. Thermal characterization demonstrated that all samples are thermally stable above 450 °C, with distinct decomposition and crystallization events associated with Ni incorporation. FTIR analysis confirmed Zn–O stretching vibrations alongside surface hydroxyl groups and residual carbon-related species. Magnetic studies evidenced weak but clear room-temperature ferromagnetism in all samples, consistent with dilute magnetic semiconductor behavior. The maximum saturation magnetization (0.117 emu g^{-1}) was observed at 15% Ni, attributed to an optimal balance between Ni^{2+} substitution, intrinsic defects, and limited secondary phase contributions. Magnetic hyperthermia measurements revealed that $Zn_{0.85}ONi_{0.15}$ nanoparticles exhibit superior heating performance, with SAR values of ~ 9.2 W g^{-1}, reaching the therapeutic threshold of 42 °C under AMF exposure. Overall our results demonstrate that $Zn_{1-X}ONi_X$ nanocomposites exhibit a relatively good magnetothermal response under an AMF, highlighting their potential relevance for magnetically assisted biomedical applications. However, further optimization is required, particularly with respect to colloidal stability and

biocompatibility, which can be addressed through appropriate surface functionalization. Future work will therefore focus on polymeric coatings, such as chitosan, to improve dispersion, mitigate dipolar aggregation, and systematically assess their influence on magnetothermal performance under optimized field conditions.

Conflicts of interest

There are no conflicts to declare.

Data availability

All authors declare that all data of the paper are available on request.

References

1 B. Xia, W. Lenggoro and K. Okuyama, Novel route to nanoparticle synthesis by salt-assisted aerosol decomposition, *Adv. Mater.*, 2001, **13**, 1579–1582, DOI: 10.1002/1521-4095(200110)13:20<1579::aid-adma1579>3.0.co;2-g.

2 M. Aamir, T. Adhikari, M. Sher, N. Revaprasadu, W. Khalid, J. Akhtar and J.-M. Nunzi, Fabrication of planar heterojunction CsPbBr2I perovskite solar cells using ZnO as an electron transport layer and improved solar energy conversion efficiency, *New J. Chem.*, 2018, **42**, 14104–14110, DOI: 10.1039/C8NJ02238K.

3 E. Mohammadi, M. Aliofkhazraei, M. Hasanpoor and M. I. Chipara, Hierarchical and complex ZnO nanostructures by microwave-assisted synthesis: morphologies, growth mechanism and classification, *Crit. Rev. Solid State Mater. Sci.*, 2018, **43**, 475–541, DOI: 10.1080/10408436.2017.1397501.

4 A. Samanta, M. N. Goswami and P. K. Mahapatra, Magnetic and electric properties of Ni-doped ZnO nanoparticles exhibit diluted magnetic semiconductor in nature, *J. Alloys Compd.*, 2018, **730**, 399–407, DOI: 10.1016/j.jallcom.2017.09.334.

5 S. Kerli, U. Alver, A. Tanriverdi and B. Avar, Structural and physical properties of boron doped ZnO films prepared by chemical spray pyrolysis method, *Crystallogr. Rep.*, 2015, **60**(6), 946–950, DOI: 10.1134/S1063774515060139.

6 M. Baneto, Y. Lare, L. Cattin, M. Addou, K. Jondo, M. Morsli and J. C. Bernede, Comparison of the Structural and Morphological Properties of Sn Doped ZnO Films Deposited by Spray Pyrolysis and Chemical Bath Deposition, *Asian J. Mater. Sci.*, 2010, **2**(4), 196–203, DOI: 10.3923/ajmskr.2010.196.203.

7 J. Cui, Zinc oxide nanowires, *Mater. Charact.*, 2012, **64**, 43–52, DOI: 10.1016/j.matchar.2011.11.017.

8 K. A. Wahid, W. Y. Lee, H. W. Lee, A. S. Teh, D. C. S. Bien and I. A. Azid, Effect of seed annealing temperature and growth duration on hydrothermal ZnO nanorod structures and their electrical characteristics, *Appl. Surf. Sci.*, 2013, **283**, 629–635, DOI: 10.1016/j.apsusc.2013.06.159.

9 G. Z. Xing, X. S. Fang, Z. Zhang, D. D. Wang, X. Huang, J. Guo and T. Wu, Ultrathin single-crystal ZnO nanobelts: Ag-catalyzed growth and field emission property, *Nanotechnology*, 2010, **21**(25), 255701, DOI: 10.1088/0957-4484/21/25/255701.

10 T. Iqbal, M. A. Khan and H. Mahmood, Facile synthesis of ZnO nanosheets: structural, antibacterial, and photocatalytic studies, *Mater. Lett.*, 2018, **224**, 59–63, DOI: 10.1016/j.matlet.2018.04.078.

11 M. Naseer, U. Aslam, B. Khalid and B. Chen, Green route to synthesize zinc oxide nanoparticles using leaf extracts of Cassia fistula and Melia azadarach and their antibacterial potential, *Sci. Rep.*, 2020, **10**(1), 9055, DOI: 10.1038/s41598-020-65949-3.

12 S. Raha and M. Ahmaruzzaman, ZnO nanostructured materials and their potential applications: progress, challenges and perspectives, *Nanoscale Adv.*, 2022, **4**, 1868–1925, DOI: 10.1039/D1NA00880C.

13 W. Wei, H. Shoulong, Z. Fuchun, W. Xiaoyang, Z. Shuili, Y. Junfeng and Z. Weihu, Fabrication and Study on Magnetic-Optical Properties of Ni-Doped ZnO Nanorod Arrays, *Micromachines*, 2019, **10**, 622, DOI: 10.3390/mi10090622.

14 Y. Zaman, et al, Modified physical properties of Ni doped ZnO NPs as potential photocatalyst and antibacterial agents, *Arab. J. Chem.*, 2023, **16**, 105230, DOI: 10.1016/j.arabjc.2023.105230.

15 S. M. Mustafa, A. A. Barzinjy, A. H. Hamad and S. M. Hamad, Green synthesis of Ni doped ZnO nanoparticles using dandelion leaf extract and its solar cell applications, *Ceram. Int.*, 2022, **48**(19), 29257–29266, DOI: 10.1016/j.ceramint.2022.05.202.

16 M. Xu, Q. Li, Y. Ma and H. Fan, Ni-doped ZnO nanorods gas sensor: enhanced gas-sensing properties, AC and DC electrical behaviors, *Sens. Actuators, B*, 2014, **199**, 403–409, DOI: 10.1016/j.snb.2014.03.108.

17 M. Ibrahim, K. Kannan, H. Parangusan, S. Eldeib, O. Shehata, M. Ismail and K. K. Sadasivuni, Enhanced corrosion protection of epoxy/ZnO-NiO nanocomposite coatings on steel, *Coatings*, 2020, **10**(8), 783, DOI: 10.3390/coatings10080783.

18 J. Mohapatra, D. K. Mishra, S. K. Kamilla, V. R. R. Medicherla, D. M. Phase, V. Berma and S. K. Singh, Ni-doped ZnO: studies on structural and magnetic properties, *Phys. Status Solidi B*, 2011, **248**(6), 1352–1359, DOI: 10.1002/pssb.201046513.

19 T. C. Yang, F. C. Chang, H. P. Wang, Y. L. Wei and C. J. Jou, Photocatalytic splitting of seawater effected by (Ni- ZnO) @C nanoreactors, *Mar. Pollut. Bull.*, 2014, **85**(2), 696–699, DOI: 10.1016/j.marpolbul.2014.02.011.

20 G. Rizwana, K. I. Talib, A. N. Jamal, i. G. Shil, A. Ghafar, B. Imed and R. Ziaur, *RSC Adv.*, 2025, **15**, 11587, DOI: 10.1039/d5ra00728c.

21 P. E. Le Renard, O. Jordan, A. Faes, A. Petri-Fink, H. Hofmann, D. Rüfenacht, F. Bosman, F. Buchegger and E. Doelker, The in vivo performance of magnetic particle-loaded injectable, in situ gelling, carriers for the delivery of local hyperthermia, *Biomaterials*, 2010, **31**, 691–705.

22 Z. Hedayatnasab, F. Abnisa and W. M. A. W. Daud, Review on magnetic nanoparticles for magnetic nanofluid hyperthermia application, *Mater. Des.*, 2017, **123**, 174–196.

23 A. Jordan, P. Wust, H. Fähling, W. John, A. Hinz and R. Felix, Inductive heating of ferrimagnetic particles and magnetic fluids: physical evaluation of their potential for hyperthermia, *Int. J. Hyperthermia*, 2009, **25**(7), 499–511.

24 E. Kita, S. Hashimoto, T. Kayano, M. Minagawa, H. Yanagihara, M. Kishimoto, K. Yamada, T. Oda, N. Ohkohchi and T. Takagi, Heating characteristics of ferromagnetic iron oxide nanoparticles for magnetic hyperthermia, *J. Appl. Phys.*, 2010, **107**(9), 09B321.

25 E. AlMatri, N. Madkhali, S. Mustafa, O. M. Lemine, S. Algessair, A. Mustafa, R. Ali and K. El-Boubbou, Preparation, Characterization, and Antibacterial Activity of Various Polymerylated Divalent Metal-Doped MF_2O_4 (M = Ni, Co, Zn) Ferrites, *Polymers*, 2025, **17**, 1171, DOI: 10.3390/polym17091171.

26 O. M. Lemine, N. Al-Dosari, S. Algessair, *et al.*, Tuning the physical properties of ternary alloys (NiCuCo) for in vitro magnetic hyperthermia: experimental and theoretical investigation, *Sci. Rep.*, 2024, **14**, 25059, DOI: 10.1038/s41598-024-76615-3.

27 S. Jeyachandran, H. Chellapandian and N. Ali, Advancements in Composite Materials and their Expanding Role in Biomedical Applications, *Biomimetics*, 2023, **8**, 518, DOI: 10.3390/biomimetics8070518.

28 B. Y. Oh, M. C. Jeong, D. S. Kim, W. Lee and J. M. Myoung, Post-annealing of Al-doped ZnO films in hydrogen atmosphere, *J. Cryst. Growth*, 2005, **281**, 475–480, DOI: 10.1016/j.jcrysgro.2005.04.045.

29 D. Nipane, S. R. Thakare and N. T. Khati, Synthesis of novel ZnO having cauliflower morphology for photocatalytic degradation study, *J. Catal.*, 2013, **2013**, 1–8, DOI: 10.1155/2013/940345.

30 S. Mahalakshmi, N. Hema and P. P. Vijaya, Hi In vitro biocompatibility and antimicrobial activities of zinc oxide nanoparticles (ZnO NPs) prepared by chemical and green synthetic route—a comparative study, *BioNanoScience*, 2020, **10**(1), 112–121, DOI: 10.1007/s12668-019-00698-w.

31 S. Crispi and G. Neri, Development of a Conductometric Sensor Based on Al, Ca-Doped ZnO for the Detection of Formaldehyde, *Sensors*, 2022, **22**(19), 7465, DOI: 10.3390/s22197465.

32 L. A. Saghatforoush, M. Hasanzadeh, S. Sanati and R. Mehdizadeh, Ni(OH)2 and NiO nanostructures: synthesis, characterization and electrochemical performance, *Bull. Kor. Chem. Soc.*, 2012, **33**, 2613–2618, DOI: 10.5012/bkcs.2012.33.8.2613.

33 M. A. Gondal, T. A. Saleh and Q. A. Drmosh, Synthesis of nickel oxide nanoparticles using pulsed laser ablation in liquids and their optical characterization, *Appl. Surf. Sci.*, 2012, **258**, 6982–6986, DOI: 10.1016/j.apsusc.2012.03.1477.

34 A. K. Rana, Y. Kumar, P. Rajput, S. N. Jha, D. Bhattacharyya and P. M. Shirage, Search for origin of room temperature

ferromagnetism properties in Ni-doped ZnO nanostructure, *ACS Appl. Mater. Interfaces*, 2017, **9**(8), 7691–7700, DOI: 10.1021/acsami.6b12616.

35 S. Fabbiyola, V. Sailaja, L. John Kennedy, M. Bououdina and j. Judith Vijaya, Optical and magnetic properties of Ni-doped ZnO nanoparticles, *J. Alloys Compd.*, 2016, **694**, 522–531, DOI: 10.1016/j.jallcom.2016.10.022.

36 O. M. Lemine, A. Modwi, A. Houas, *et al.*, Room temperature ferromagnetism in Ni, Fe and Ag co-doped Cu–ZnO nanoparticles: an experimental and first-principles DFT study, *J. Mater. Sci.: Mater. Electron.*, 2018, **29**, 14387–14395, DOI: 10.1007/s10854-018-9571-5.

37 A. Sabik, M. R. Elamin, O. M. Lemine, M. Alshammari, M. Hjiri, T. Attoub, *et al.*, Assessing the Heating Ability of Carbon Nanotubes-Fe_3O_4 Nanocomposites for Magnetic

Hyperthermia Application, *J. Nano Res.*, 2024, **86**, 1–13, DOI: 10.4028/p-wb5gsx.

38 O. M. Lemine, *et al.*, Structure, magnetism and heating ability of pyrrole-functionalized magnetic biochar (PFMB) for magnetic hyperthermia, *RSC Adv.*, 2025, **15**(34), 28145–28154.

39 F. Re yes-Ortega, *et al.*, Magnetic Nanoparticles Coated with a Thermosensitive Polymer with Hyperthermia Properties, *Polymers*, 2018, **10**(1), 10.

40 E. Catalano and A. Di Benedetto, IOP Conf. Series, *J. Phys.:Conf. Ser.*, 2017, **841**, 012010.

41 S. Algessair, *et al.*, Tuning the heat dissipated by polyacrylic acid (PAA)-coated magnetite nanoparticles under alternating magnetic field for hyperthermia applications, *Appl. Phys. A:Mater. Sci. Process.*, 2023, **129**, 814.